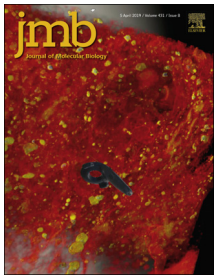

Roles of the Hydrophobic Gate and Exit Channel in *Vigna radiata* Pyrophosphatase Ion Translocation

Jia-Yin Tsai [1], Kai-Zhi Tang [1], Kun-Mou Li [1], Bo-Ling Hsu [1], Yun-Wei Chiang [2], Adrian Goldman [3,4] and Yuh-Ju Sun [1]

*1 - **Department of Life Science and Institute of Bioinformatics and Structural Biology,** National Tsing Hua University, Hsinchu 30013, Taiwan*
*2 - **Department of Chemistry,** National Tsing Hua University, Hsinchu 30013, Taiwan*
*3 - **Astbury Centre for Structural Molecular Biology,** School of Biomedical Sciences, University of Leeds, Leeds LS2 9JT, England*
*4 - **Division of Biochemistry,** Department of Biosciences, University of Helsinki, Helsinki FIN-00014, Finland*

***Correspondence to Yuh-Ju Sun:** Department of Life Science and Institute of Bioinformatics and Structural Biology, National Tsing Hua University, Hsinchu 30013, Taiwan. yjsun@life.nthu.edu.tw*
https://doi.org/10.1016/j.jmb.2019.03.009
Edited by Nieng Yan

Abstract

Membrane-embedded pyrophosphatase (M-PPase) hydrolyzes pyrophosphate to drive ion (H^+ and/or Na^+) translocation. We determined crystal structures and functions of *Vigna radiata* M-PPase (*Vr*H^+-PPase), the *Vr*H^+-PPase–$2P_i$ complex and mutants at hydrophobic gate (residue L555) and exit channel (residues T228 and E225). Ion pore diameters along the translocation pathway of three *Vr*H^+-PPases complexes (P_i-, $2P_i$- and imidodiphosphate-bound states) present a unique wave-like profile, with different pore diameters at the hydrophobic gate and exit channel, indicating that the ligands induced pore size alterations. The $2P_i$-bound state with the largest pore diameter might mimic the hydrophobic gate open. In mutant structures, ordered waters detected at the hydrophobic gate among *Vr*H^+-PPase imply the possibility of solvation, and numerous waters at the exit channel might signify an open channel. A salt-bridge, E225–R562 is at the way out of the exit channel of *Vr*H^+-PPase; E225A mutant makes the interaction eliminated and reveals a decreased pumping ability. E225–R562 might act as a latch to regulate proton release. A water wire from the ion gate (R-D-K-E) through the hydrophobic gate and into the exit channel may reflect the path of proton transfer.

Introduction

Membrane-embedded pyrophosphatases (M-PPases) (E.C. 3.6.1.1) are unique ion pumps that hydrolyze pyrophosphate (PP_i) to drive H^+ and/or Na^+ transport across vacuolar or plasma membranes against the electrochemical gradient [1,2]. PP_i is a biosynthetic by-product of NTP-dependent biosynthesis, for example, DNA, RNA, protein, starch, cellulose and fatty acid synthesis [2–4]. All M-PPases require Mg^{2+} to activate enzymatic functions and as a cofactor for the formation of substrate–Mg_2–PP_i complex [5–7]. M-PPases have been discovered in all kingdoms of life, apart from fungi and animals [8–10].

M-PPases comprise a 66-90 kDa polypeptide containing 16 transmembrane helices (TMs), and it forms a dimer [2,11,12]. M-PPases are classified into two major types, K^+-dependent or K^+-independent [13,14], depending on presence of a functional determinant residue (alanine or lysine). K^+-independent M-PPases have a conserved lysine that uses the NH_3 side-chain group to occupy the K^+ position for M-PPase activation, and they can be further classified into two subfamilies based on whether or not they are regulated by Na^+ [15]. K^+-dependent M-PPases have a conserved alanine and require K^+-binding for optimal activity, and they can be further subdivided into five subfamilies for pumping H^+, Na^+ or Na^+/H^+ based on the position of a "semi-conserved glutamate" [15]. Apart from acidifying the lumen, M-PPases enhance the resistance of plants to cold, drought, salinity and many other stresses. *Arabidopsis* vacuolar proton-pumping pyrophosphatase (AVP1) can play the dual functions of PP_i synthesis and

hydrolysis to optimize P_i use efficiency during salt stress [16–18]. Binding of AVP1 to its regulatory proteins, 14-3-3 protein isoforms, increases both enzymatic activity and proton pumping ability [19]. That latter study demonstrated that 14-3-3 proteins preferentially bind to T530/TM12, T618/TM13, S638/TM14, T639/TM14 and T728/TM16 [19]. TMs 12 and 16 are core TMs directly involved in ion translocation [20]. TMs 13 and 14 are outer TMs and exhibit conformational change upon PP_i-binding/hydrolysis and P_i detachment [21].

The three-dimensional structures of plant H^+-PPase from *Vigna radiata* (*Vr*H^+-PPase) [20] and of bacterial Na^+-PPase from *Thermotoga maritima* (*Tm*Na^+-PPase) [22] have been determined. Both *Vr*H^+-PPase and *Tm*Na^+-PPase have 16 TMs and exhibit the same inner/outer rosette fold. Six core TMs (TMs 5–6, 11–12 and 15–16) face the cytosol and form the PP_i-binding pocket, linking the ion transport pathway through the hydrophobic gate and exit channel into the lumen (of plants and protozoan parasites) or the periplasm (of archaea and bacteria) [20,22,23].

The ion gate of *Vr*H^+-PPase consists of four sequential charged residues, R242–D294–K742–E301 (hereafter R-D-K-E), which lies under the PP_i-binding pocket and face the lumen [20]. The first three of these residues are highly conserved among M-PPases, but E301 is semi-conserved. For example, E246 of *Tm*Na^+-PPase is one turn higher than E301 of *Vr*H^+-PPase. *Vr*H^+-PPase uses R-D-K-E to pump protons across vacuolar membranes into the lumen [20], whereas *Tm*Na^+-PPase only uses D-K-E to execute sodium translocation across plasma membranes [22]. The hydrophobic gate and exit channel lie underneath the ion gate and near the lumen [20]. The hydrophobic gate of *Vr*H^+-PPase is formed by residues L232, A305, L555 and V746 [20], and it prevents backflow of protons from the lumen into the cytosol.

Lin *et al*. [20] reported the crystal structure of *Vr*H^+-PPase in complex with the PP_i analogue imidodiphosphate (IDP) (*Vr*H^+-PPase–IDP; PDB: 4A01), five Mg^{2+} and one K^+ as being in the initiated (substrate-bound) state. The crystal structure of ligand-free *Tm*Na^+-PPase (PDB: 4AV3) bound with one Ca^{2+} and one Mg^{2+} is in the resting state [22]. *Tm*Na^+-PPase bound to two P_i, four Mg^{2+}, and one K^+ is in the product-bound state (PDB: 4AV6) [22]. The catalytic and ion-pumping mechanism of M-PPases involves the resting state (PDB: 4AV3), IDP-bound state (PDB: 4A01 and 5LZQ), PP_i-hydrolysis transient state, PP_i-hydrolyzed state, $2P_i$ product-bound state (PDB: 4AV6) and P_i-released state (PDB: 5GPJ and 5LZR) [20–22]. In a previous comprehensive study, we established the order of ion pumping and PP_i hydrolysis during the catalytic cycle, revealing that binding of a non-hydrolyzable PP_i analogue (IDP) could induce a single turnover ion-pumping event, although the specific mechanism and dynamic conformational change remain unclear. Since the R-D-K-E ion gate, hydrophobic gate and exit channel are closed in all the solved structures of *Vr*H^+-PPase [20] and *Tm*Na^+-PPase [22], the mechanism of how PP_i hydrolysis is linked to ion translocation remains uncertain.

In this study, we investigate the structural and functional importance of the hydrophobic gate and exit channel of the ion transport pathway of *Vr*H^+-PPase. We determined the crystal structure of the *Vr*H^+-PPase–$2P_i$ complex and mutants (E301Q, L555M/K, T228D and E225A/S/H) in the hydrophobic gate and exit channel. We analyzed the ion pores along the transport pathway of various *Vr*H^+-PPase conformational states. We also assessed pyrophosphate hydrolysis and proton pumping activities of these mutants. We show that the hydrophobic gate can be hydrated, and that the E225–R562 salt-bridge at the exit channel might be essential for proton release by *Vr*H^+-PPase.

Results

The *Vr*H^+-PPase–$2P_i$ complex

To mimic the PP_i hydrolyzed state, we grew crystals of the *Vr*H^+-PPase–$2P_i$ complex. They diffracted to a resolution of 2.3 Å (Table 1). We determined the overall structure of *Vr*H^+-PPase–$2P_i$ (Fig. 1a) by molecular replacement, using *Vr*H^+-PPase–IDP (PDB: 4A01) [20] as a search model. *Vr*H^+-PPase–$2P_i$ shares a similar overall structure to that of *Vr*H^+-PPase–IDP [20]. We identified two free phosphates, one K^+ and five Mg^{2+} ions (Mg1–Mg5) in the PP_i-binding pocket (Figs. 1b and S1a and b). The Mg^{2+} ions play roles in enzyme function (Mg1 and Mg3), substrate binding (Mg2 and Mg4) and enzyme stabilization (Mg5) [20]. The phosphates from the hydrolyzed PP_i are an electrophilic phosphate (P1) adjacent to the putative nucleophilic water, and the distal leaving-group phosphate (P2). In our *Vr*H^+-PPase–$2P_i$ structure, P1 is coordinated by K250, K730 and three Mg^{2+} ions (Mg3, Mg4 and Mg5), whereas P2 is firmly fixed by K694 and all five Mg^{2+} ions (Fig. 1b). The interactions of the Mg^{2+} ions with P2 are stronger than those with P1, so P1 is the first to leave the binding pocket after PP_i hydrolysis, as found for other inorganic pyrophosphatases (e.g., yeast pyrophosphatase Y-PPase) [24]. Structural comparison of *Vr*H^+-PPase in the IDP- and P_i-bound states revealed that P2 is in the same position in both states, whereas P1 was positioned 0.6 Å lower in the P_i-bound state than in the IDP-bound state (Fig. S1c).

In the IDP-binding pocket of *Vr*H^+-PPase–IDP [20], an essential water molecule (Wat_{nu}) was identified near P1 as a nucleophile to attack PP_i during hydrolysis [20]. However, in our *Vr*H^+-PPase–$2P_i$ complex, Wat_{nu} is absent and its position is occupied by the descending P1 (Fig. 1b). The product-bound state of Y-PPase has

Table 1. Data collection and refinement statistics of the *Vr*H$^+$-PPase–2P$_i$ complex and *Vr*H$^+$-PPase mutant crystals

Crystal	2Pi-bound	E301Q	L555M	L555K	T228D	E225A	E225S	E225H
Space group	*C*2	*C*2	*C*2	*C*2	*C*2	*C*2	*C*2	*C*2
Cell dimensions (Å)								
a	217.6	217.2	221.2	221.3	212.7	217.2	218.1	215.6
b	88.4	88.3	88.4	88.6	88.1	88.3	88.2	88.0
c	159.1	158.7	159.7	161.1	156.7	158.8	158.9	158.2
β (°)	125.5	125.3	125.7	126.1	124.5	125.1	125.4	125.0
Resolution (Å)[a]	30.00–2.30	30.00–2.50	30.00–2.80	30.00–2.70	30.00–2.20	30.0–2.30	30.00–2.40	30.00–2.48
R_{meas} (%)[a]	9.7 (170.0)	8.8 (31.6)	9.9 (51.5)	12.8 (128.3)	9.3 (120.9)	7.6 (76.5)	10.7 (134.7)	10.8 (112.9)
R_{merge} (%)[a,b]	8.3 (146.8)	7.5 (26.7)	8.6 (44.7)	11.1 (110.9)	7.9 (100.6)	7.1 (70.7)	9.1 (114.5)	9.4 (97.3)
I/σ[a]	13.8 (1.4)	16.3 (2.5)	16.8 (2.8)	12.0 (1.2)	12.0 (1.1)	26.9 (2.2)	12.6 (1.2)	13.9 (1.1)
Completeness[a] (%)	96.2 (94.0)	96.1 (81.6)	99.0 (93.8)	99.6 (97.5)	97.2 (90.1)	99.0 (92.0)	91.7 (81.6)	97.4 (83.4)
Redundancy[a]	3.9 (3.7)	3.6 (3.3)	4.2 (3.9)	4.1 (3.8)	3.5 (2.9)	7.5 (6.4)	3.5 (3.3)	4.1 (3.5)
$CC_{1/2}$	0.696	0.945	0.922	0.681	0.685	0.885	0.657	0.616
Refinement								
Resolution range (Å)	2.30	2.50	2.80	2.70	2.20	2.30	2.40	2.48
No. reflections	104,814	81,592	61,309	68,484	118,542	141,563	87,856	82,958
R_{work} (%)/R_{free} (%)	20.7/24.0	17.6/20.8	18.2/22.9	19.7/23.9	19.9/23.5	16.5/19.9	19.1/22.6	20.1/23.5
No. atoms	11,406	11,515	11,197	11,215	11,549	11,489	11,351	11,218
Protein	10,855	10,862	10,862	10,864	10,864	10,854	10,856	10,864
(no. of residues)	(1480)	(1480)	(1480)	(1480)	(1480)	(1480)	(1480)	(1480)
P$_i$	20 (4 P$_i$)	20 (4P$_i$)	20 (4 P$_i$)	20 (4 P$_i$)	20 (4 P$_i$)	20 (4 P$_i$)	20 (4 P$_i$)	20 (4 P$_i$)
Mg	10	10	10	10	10	10	10	10
K	2	2	2	2	2	2	2	2
H_2O	400	502	235	217	534	488	361	210
PEG2KMME	119	119	68	102	119	115	102	112
B-factors (Å^2)								
All atoms	42.91	20.44	21.09	53.60	42.55	24.33	21.88	50.58
Protein	42.69	20.13	21.10	53.45	42.27	23.40	21.76	50.49
P$_i$	37.93	15.75	23.41	56.96	36.76	15.38	16.25	47.56
Mg	39.74	17.03	18.58	54.39	36.92	15.70	16.89	47.88
K	49.66	21.06	23.37	75.88	50.78	22.06	24.21	56.13
H_2O	44.47	23.24	17.40	53.09	44.93	27.67	21.34	46.71
PEG2KMME	58.18	38.84	32.39	69.20	59.25	43.46	37.88	67.11
R.M.S deviations								
Bond length (Å)	0.008	0.007	0.008	0.008	0.007	0.008	0.008	0.008
Bond angle (°)	1.121	1.043	1.158	1.139	1.071	1.065	1.173	1.144

[a] Values in the parenthesis are for the highest-resolution shell.
[b] $R_{merge} = \Sigma \mid I - \langle I \rangle \mid / \Sigma I$, where I = observed intensity and $\langle I \rangle$ = average intensity from multiple observation of symmetry related reflections.

been identified as either in an immediate or relaxed state based on the up or down orientation of P1 [24]. In our *Vr*H$^+$-PPase–2P$_i$ crystal structure, PP$_i$ has been hydrolyzed into two phosphates (P1 and P2), and P1 is in the downward position where it occupies the corresponding location of Wat$_{nu}$ in the *Vr*H$^+$-PPase–IDP complex, suggesting that it is in an immediate product-bound state (Fig. 1b).

E301Q mutant in ion gate

Ion translocation by *Vr*H$^+$-PPase from cytosol to lumen is coupled with PP$_i$ hydrolysis via the four R-D-K-E charged residues [20]. Residue E301 is located between the ion gate and hydrophobic gate of M-PPases, and it functions as a proton acceptor/donor (Fig. 2a). E301 is highly conserved in plant H$^+$-PPases, and previous mutagenesis studies have shown that mutation of E301 abolishes PP$_i$ hydrolysis and proton translocation; for example, E305Q in AVP1 [25] and E301A in *Vr*H$^+$-PPase [26]. We found that the PP$_i$ hydrolysis activity of the E301Q mutant was half that of the wild type, and proton pumping activity was undetectable (Fig. 2b and Table 2).

We determined the crystal structure of the E301Q mutant at a resolution of 2.7 Å and found that it exhibits a similar interaction to that of *Vr*H$^+$-PPase–2P$_i$ (Fig. 3a). Although the side-chain orientation of Q301 is the same as that of E301 (Fig. 3b), the glutamine cannot be protonated and deprotonated like E301. Because the side-chains of E301 and K742 exhibit acid–base pair interactions in the *Vr*H$^+$-PPase–P$_i$ complex during the pumping process (Fig. 3c) [21], the Q301 side-chain in the mutant enzyme complex forms a hydrogen bond with the main chain of K742 that might fix the flexibility of Q301 and thus affect its proton pumping activity (Fig. 3b).

Proton transportation is facilitated through coordinated water molecules in the form of a water wire, such as observed in bacteriorhodopsin [28], cytochrome *c*

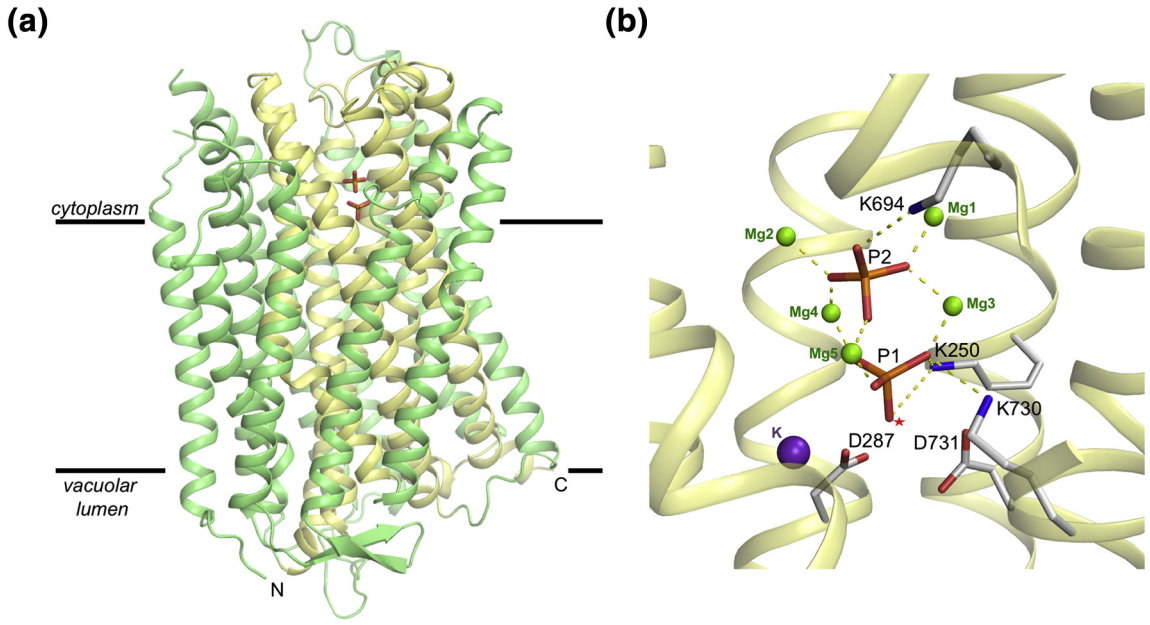

Fig. 1. Overall structure of the *Vr*H$^+$-PPase–2P$_i$ complex. (a) Structural overview of the *Vr*H$^+$-PPase–2P$_i$ complex, with core TMs in yellow and outer TMs in green. P$_i$ is presented as CPK-colored sticks. (b) Zoom-in the binding pocket of the *Vr*H$^+$-PPase–2P$_i$ complex. The two phosphates are bonded with metal ions and three Lys residues. The red asterisk represents the position of the previously described nucleophilic water in the *Vr*H$^+$-PPase–IDP complex (PDB: 4A01) [20].

oxidase [29] and the *Vr*H$^+$-PPase–IDP complex [20]. In the ion translocation pathway of the *Vr*H$^+$-PPase–IDP complex [20], several functional waters were identified, including the nucleophile water (Wat$_{nu}$) and two ordered waters (Wat1 and Wat2) along the R-D-K-E ion gate. Surprisingly, we also found two ordered water molecules (Wat3 and Wat4) in the hydrophobic gate of the E301Q mutant, which were coordinated with each other and bonded with the C=O backbones of T228 (Wat3) and Q301 (Wat4) (Fig. 3b). Wat3 and Wat4 have not previously been reported in the hydrophobic gates of M-PPases and could reflect how a proton transferred through the water wire from the ion gate to the hydrophobic gate. Wat3 and Wat4 are located at the hydrophobic gate in the E301Q mutant, suggesting the possibility that this gate in *Vr*H$^+$-PPase becomes solvated during proton translocation.

L555M and L555K mutants in the hydrophobic gate

Lying below the R-D-K-E ion gate is the *Vr*H$^+$-PPase hydrophobic gate formed by residues L232, A305, L555 and V746 [20] (Fig. 2a). L555 of TM12 is highly conserved among M-PPases. In *Vr*H$^+$-PPase, L555 mutants show distinct PP$_i$ hydrolysis and proton-pumping abilities, with L555A mutation uncoupling these two activities and L555D being inactive [27]. To investigate the influence of polarity and residue size at the hydrophobic gate, we generated L555M and L555K mutants (Fig. 2c). The PP$_i$-hydrolytic activity of the L555M mutant is 75% that of wild type, and its proton-pumping activity is rather low (29% that of wild type) (Fig. 2b and Table 2). The PP$_i$-hydrolytic activity of the L555K mutant is even lower (44% of wild type), and we could not detect any proton-pumping activity for this mutant (Fig. 2b). Thus, L555 mutation significantly affects the proton-pumping ability of *Vr*H$^+$-PPase.

The crystal structures of the L555M and L555K mutants, determined at resolutions of 2.8 and 2.7 Å, respectively (Table 1), are essentially the same as that of the *Vr*H$^+$-PPase–2P$_i$ complex. In the L555M structure, residue M555 forms an interaction with E301 over a distance of 3.7 Å (Fig. 3d), which might restrict the flexibility of E301 and affect its functional role in proton translocation. In addition, the water molecule (Wat3) is recruited near the hydrophobic gate of the L555K mutant (Fig. 3e) and is coordinated by residues T228, E301 and K555, as also observed in our E301Q structure (Fig. 3b). Therefore, residue L555 is important for the proton-pumping and transport activity of *Vr*H$^+$-PPase and, likely other M-PPases, because of its size and properties.

T228D and E225A/E225S/E225H mutants in exit channel

To facilitate ion translocation into the lumen from the exit channel, the binding affinity of the exit channel for ions might be lower than in the translocation pathway inside the membrane [20,23]. M-PPases exhibit a diversity of residues around their exit channels (Fig. 2c), including polar and charged amino acids (such as E225, T228 and R562 in *Vr*H$^+$-PPase) facing the

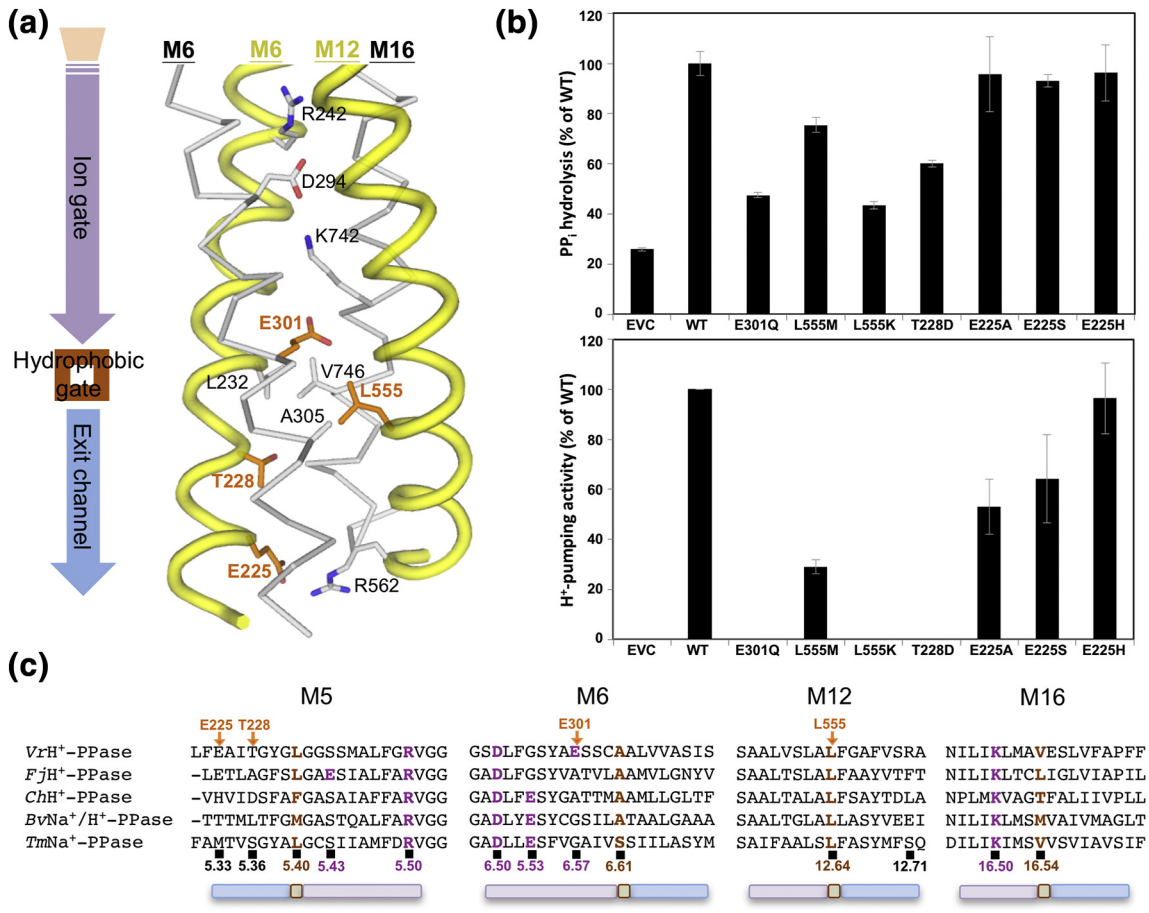

Fig. 2. Enzyme activities of *Vr*H$^+$-PPase mutants. (a) Sub-structure of *Vr*H$^+$-PPases under the PP$_i$-hydrolytic pocket. Critical residues involved in ion translocation include R242, D294, K742 and E301. Important residues of the hydrophobic gate include L232, A305, L555 and V746. Crucial exit channel residues include E225, T228 and R562. Residues in orange were selected for mutagenesis, that is, E301Q, L555M/K, T228D and E225A/S/H. (b) PP$_i$-hydrolytic activities (upper) and proton-pumping activities (lower) of *Vr*H$^+$-PPase mutants. Error bars represent the standard error of the mean (n = 3). (c) Primary sequence alignment of four TMs (TMs 5, 6, 12 and 16) from five K$^+$-dependent M-PPases: *V. radiata* H$^+$-PPase (*Vr*H$^+$-PPase) *F. johnsoniae* H$^+$-PPase (*Fj*H$^+$-PPase), *C. hydrogenoformans* H$^+$-PPase (*Ch*H$^+$-PPase), *B. vulgatus* Na$^+$/H$^+$-PPase (*Bv*Na$^+$/H$^+$-PPase) and *T. maritima* Na$^+$-PPase (*Tm*Na$^+$-PPase). The TM helices are shown above the sequence alignment. The ion gate, hydrophobic gate and exit channel are shown as lines under the sequence and are colored blue, brown and purple, respectively. The black boxes under residues represent the Ballesteros and Weinstein numbered nomenclature [23]. Arrows above the sequence point to residues mutated in this study.

center of the exit channel. Residues E225 and T228 lie in TM5, with T228 located one helix turn below the hydrophobic gate to link it to the exit channel, and as the residue in TM5 nearest the lumen, E225 forms a salt-bridge with R562 that might play a role in proton release to the lumen (Fig. 2a and c) [20]. To investigate the role

Table 2. PP$_i$ hydrolysis and proton pumping activities of *Vr*H$^+$-PPase mutants

Residues in *Vr* H$^+$-PPase	Mutation	PPi hydrolysis (% of WT)	Proton pumping (% of WT)	Coupling ratio (% of WT)	References
Ion gate	E301Q	48	0	–	This work
Hydrophobic gate	L555A	39	0	–	[27]
	L555D	0	0	–	[27]
	L555M	75	29	38	This work
	L555K	44	0	–	This work
Exit channel	T228D	60	0	–	This work
	E225A	95	53	55	This work
	E225S	93	64	68	This work
	E225H	96	96	100	This work

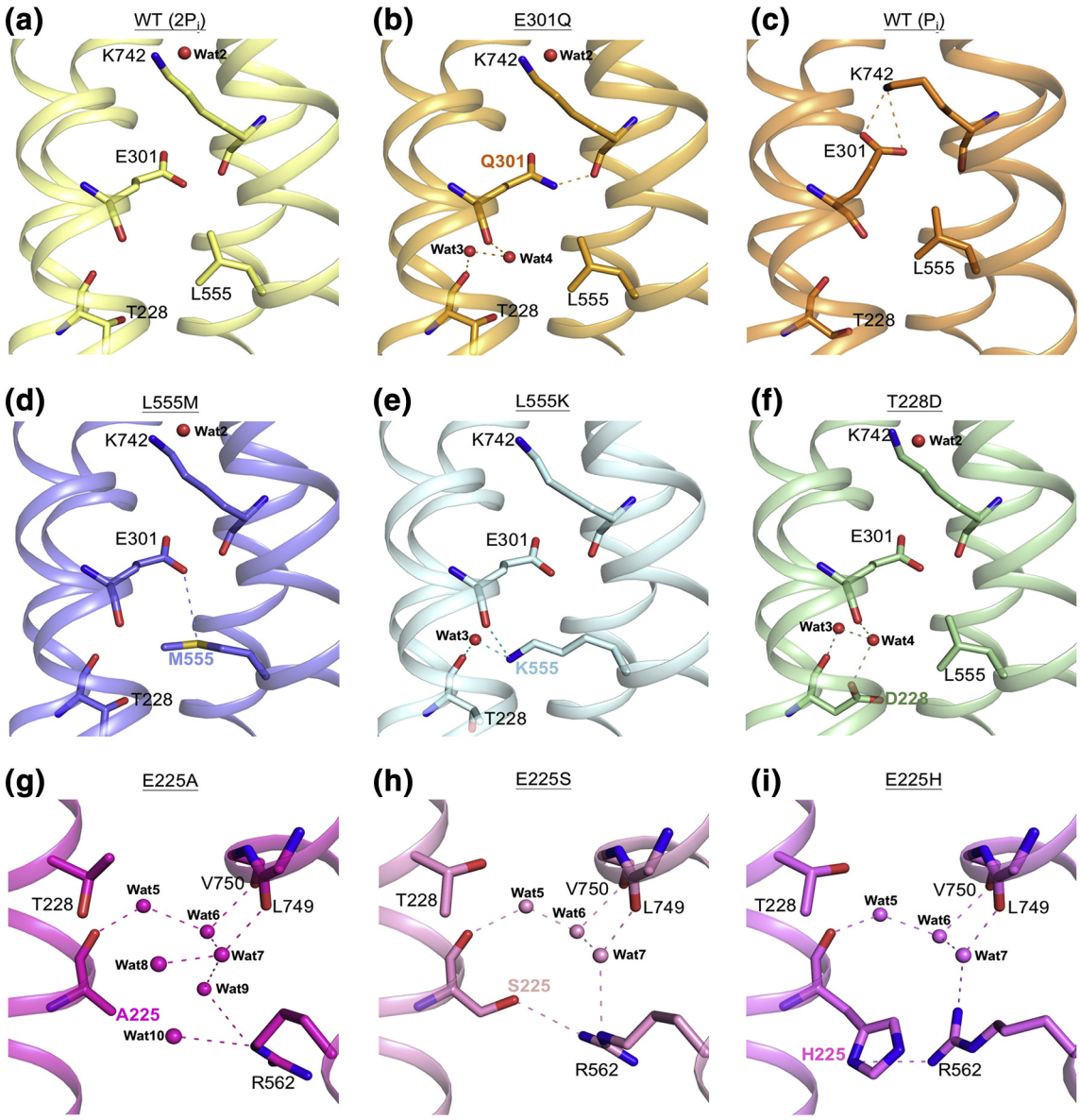

Fig. 3. Structural comparison of *Vr*H$^+$-PPase and various mutants. The hydrophobic gates of the (a) *Vr*H$^+$-PPase–2P$_i$ complex, (b) E301Q mutant, (c) *Vr*H$^+$-PPase–P$_i$ complex, (d) L555M mutant, (e) L555K mutant and (f) T228D mutant. The exit channels of the (g) E225A mutant, (h) E225S mutant and (i) E225H mutant. Mutant residues are shown as sticks, and red spheres represent water molecules. The dashed lines indicate H-bond interactions.

of polar residues along the exit channel, we generated T228D and E225A/S/H mutants. We found that the T228D mutant maintained 60% of the PP$_i$-hydrolytic activity of wild type, but exhibited no proton-pumping activity (Fig. 2b). The E225A mutant had 95% of the PP$_i$ hydrolytic activity and 53% of the proton-pumping activity of wild type (Fig. 2b). The E225S and E225H mutants had 93% and 96% of the PP$_i$ hydrolytic activities of wild type, respectively, and 64% and 96% of its proton-pumping activity, respectively (Fig. 2b and Table 2).

We determined the crystal structures of the T228D, E225A, E225S and E225H mutants and found that they share a similar overall structure to that of the *Vr*H$^+$-PPase–2P$_i$ complex (Table 1). In the T228D structure at a resolution of 2.2 Å, the D228 side-chain (which is larger than that of T228) is rotated upward toward the hydrophobic gate, so the space in the exit channel is constricted and L555 is slightly closer to D228 (Fig. 3f). In addition, we observed two waters (Wat3 and Wat4) around the hydrophobic gate in the T228D structure, coordinated by the E301 C=O backbone and D228 (its side-chain and C=O backbone) (Fig. 3f). These waters lie at similar positions in the E301Q and L555K mutants, with Wat4 located at the position of the Nζ group of residue K555 in the

L555K mutant (Fig. 3b and e). The preserved waters (Wat3 and Wat4) in the hydrophobic gates of the E301Q, L555K and T228D mutants may reveal the route of ion translocation, representing a potential water wire.

The essential E225–R562 salt-bridge found in *Vr*H$^+$-PPase complexes [20,21] was abolished in our E225A crystal structure (Fig. 3g). However, this interaction was replaced by hydrogen bonds in the crystal structures of E225S and E225H, with the Nε of the R562 side-chain interacting with the OH of the S225 side-chain (4.5 Å) (Fig. 3h) or the ND1 of the H225 side-chain (4.0 Å) (Fig. 3i). These results suggest that R562 in TM12 has a degree of flexibility in forming interactions with other charged residues in *Vr*H$^+$-PPase that are required to stabilize TM5 and TM12.

Moreover, in our E225A structure, residue A225 is unable to interact with R562, resulting in a cavity between them (Fig. 3g). We identified water molecules (Wat 8, Wat9 and Wat10) in between A225 and R562 that move through the exit channel and penetrate into this cavity, contributing to a continuous water network (Wat5, Wat6, Wat7, Wat8, Wat9, and Wat10) in the exit channel (Fig. 3g).

Ligand-induced changes in ion pore size

The proton transport pathway of *Vr*H$^+$-PPase is formed by six core TMs (TMs 5–6, 11–12 and 15–16). Using the program PoreWalker [30], pore size of the ion translocation pathway has been analyzed for various functional states, including 2P$_i$-bound (corresponding to the immediate product-bound state, this work), IDP-bound [20], and P$_i$-bound [21]. We calculated pore diameters along the ion translocation pathway, and their profiles are depicted in Fig. 4. We observed both narrow and wide pore sizes along the ion translocation pathway of the membrane portion, exhibiting a wave-like profile. The 2P$_i$-bound state presents a more wavy profile than the IDP- and P$_i$-bound states, and notably, the ion pore at D294/E301/T228 is as narrow as ~1 Å and as wide as ~4 Å at R242/K742/L555 (Fig. 4a). The pore size profile of the IDP-bound state is similar to that of the 2P$_i$-bound state (Fig. 4a), but its pore sizes are generally larger, except for around the hydrophobic gate (near L555) that is narrower (2.1 Å as opposed to 3.7 for the 2P$_i$-bound state). The pore size profile of the P$_i$-bound state is rather loose, and it is much narrower at the hydrophobic gate (2.0 Å). Since TM12 of the *Vr*H$^+$-PPase–P$_i$ complex reveals a ~3.0-Å vertical shift toward the cytosol along the ion translocation pathway [21,22], the P$_i$-bound state might represent a rather dynamic and unstable conformational state. The *Vr*H$^+$-PPase–P$_i$ complex represents a scenario in which the proton has been transferred, so the hydrophobic gate should be closed to tighten the pore. Pore profiles at the ion gate (R-D-K-E) for the three conformational states are largely similar and exhibit relatively similar pore diameters. In contrast, pore diameter was notably narrowed for the IDP- and P$_i$-bound states. Thus, binding of 2P$_i$ to *Vr*H$^+$-PPase induces the hydrophobic gate to open, given that *Vr*H$^+$-PPase–2P$_i$ exhibited the biggest pore diameter.

Comparison of the pore diameter of wild-type *Vr*H$^+$-PPase–2P$_i$ complex with those of the L555M and L555K mutants (Fig. 4b) indicated that pore size profiles are similar, particularly at the ion gate, but they deviated somewhat at the hydrophobic gate and exit channel perhaps because of the mutation at the hydrophobic gate (Fig. 3a, d and e). The diameter of the pores at the hydrophobic gate of the L555M and L555K mutants decreased from 3.7 Å (wild type) to 2.6 and 0.8 Å, respectively. Accordingly, proton-pumping activities of the L555M and L555K mutants decreased to 29% that of wild type or was completely abolished, respectively. Based on all of these findings, we suggest that the hydrophobic gate is an essential checkpoint for the proton-pumping activity of *Vr*H$^+$-PPase (and other M-PPases) and that the diameter of the hydrophobic gate is adjusted to facilitate ion transport.

Discussion

Energy coupling between PP$_i$ hydrolysis and H$^+$ pumping

The energy coupling between PP$_i$ hydrolysis and proton translocation efficiency depends on the ratio of proton-pumping to PPase activity [27]. Mutations that uncouple these two activities have been generated, such as L555A and N738A in *Vr*H$^+$-PPase [27]. Mutants in which these activities are only loosely linked also exist, either exhibiting normal PPase activity but low proton-pumping (e.g., Y126A mutant) or enhanced PPase activity but low proton-pumping (e.g., C124A mutant) [27,31]. We examined the PP$_i$ hydrolysis and proton translocation activities of various other *Vr*H$^+$-PPase mutants (Table 2). T228D, E301Q and L555K generated uncoupling mutants because their PPase activity is preserved, but they lack measureable proton-pumping activity. In contrast, L555M, E225A and E225S mutants loosen the PP$_i$ hydrolysis and proton translocation relationship since PPase activity is retained but proton-pumping activity is reduced. Besides, E225H mutation maintains the same functions as wild type.

Comparison of various L555 mutants reveals that PP$_i$ hydrolysis and proton translocation are uncoupled in the L555A mutant and only loosely coupled in the L555M mutant (probably due to differences in the length of the residue). Moreover, charged mutants L555D was completely inactive [27], whereas L555K was uncoupled in PP$_i$ hydrolysis and proton translocation; in these two cases, differences to wild-type enzyme are likely due to altered residue charges.

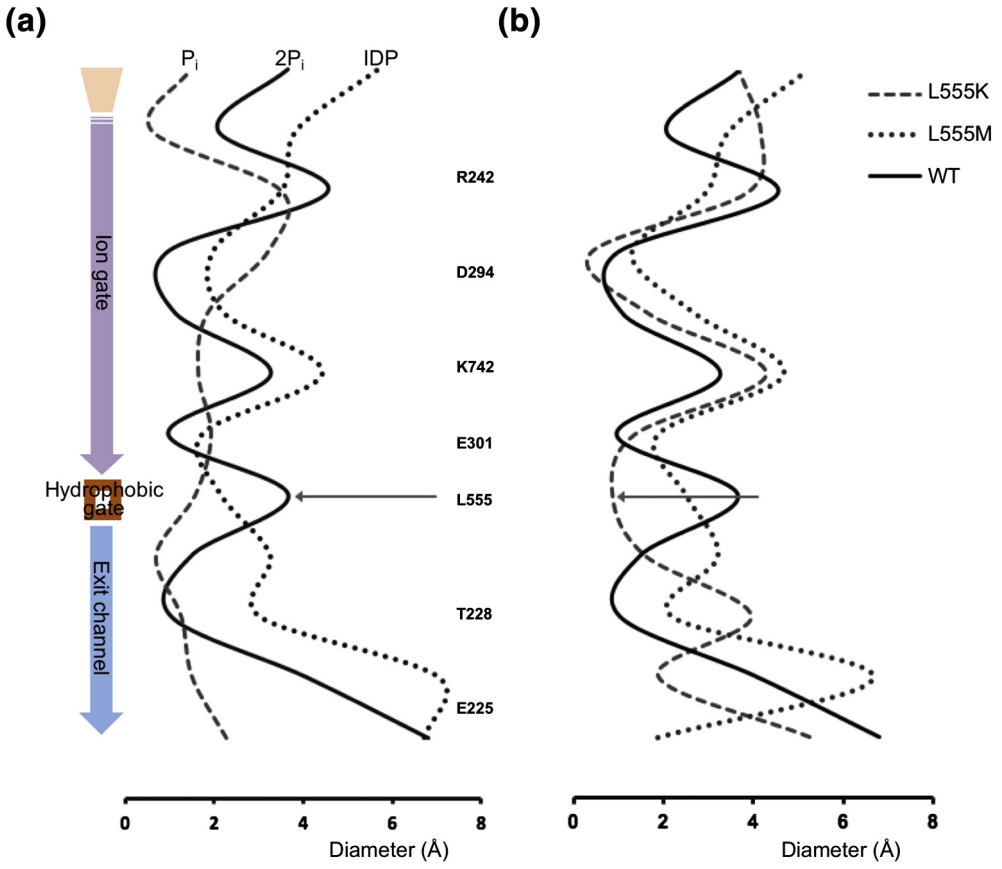

Fig. 4. Ion pore along the ion translocation pathway of *Vr*H$^+$-PPase and its mutants. Ion pore diameters of *Vr*H$^+$-PPase along the ion gate, hydrophobic gate and exit channel were calculated using PoreWalker [30]. Ion pore diameters of *Vr*H$^+$-PPase are compared among (a) the three conformational states (IDP-bound, P_i-bound and $2P_i$-bound) and (b) $2P_i$-bound and the L555M/L555K mutant structures.

Together, these findings indicate that the properties of the highly conserved L555 residue at the hydrophobic gate are critical for the PP_i hydrolysis and proton-pumping activity of *Vr*H$^+$-PPase.

A checkpoint at the hydrophobic gate

Although the diversity occurred in the exit channel, we found that the ion pore profiles of our IDP-, P_i- and $2P_i$-bound crystal structures were similar at the R-D-K-E ion gate. These highly conserved positive-negative paired residues conduct the protonation and deprotonation chain reaction for proton translocation and exhibit limited conformational change. The compact ion pore of the R-D-K-E ion gate observed in the IDP-bound and $2P_i$-bound states (Fig. 4a) may be due to D294–K742 hydrogen bond interaction and protonation of E301 to firmly close the ion gate. In contrast, lack of interaction between D294 and K742 due to the latter residue moving downward to form a hydrogen bond with deprotonated E301, as found in the P_i-bound state, may loose the ion pore (Fig. 3c).

Typically, the narrowest part of the pore is the selectivity filter in any ion transporter, such as in human aquaporin 4, AQP4 [32]. Amino acid side-chain variation has been linked to differences in pore size, for example, AtTIP2:1 [33]. M-PPases exhibit pore size adjustment at their hydrophobic gates, being narrower in both the IDP- and P_i-bound states, possibly because the proton has been transferred so that the gate is closed. However, the large pore diameter at the hydrophobic gate in the $2P_i$-bound state likely reflects the functional immediate product-bound state in which the hydrophobic gate is open. Our structural data (Fig. S2) and measurements of ion pore diameter (Fig. 4b) for the L555M/K mutants reveal that alteration of highly conserved residue L555 at the hydrophobic gate modifies the spatial volume of the gate, electrostatic charge and its pore size (Fig. 3e and f), which is in accordance with other ion channel pore diameters [34].

Certain characteristics at the critical hydrophobic gate of M-PPases allow it to act as a checkpoint; its central location in the entire ion translocation pathway, its limited spatial footprint (2.0–3.7 Å), and its high hydrophobicity. The hydrophobic gate of *Vr*H^+-PPase exhibits the unique sequence "L232$^{5.40}$–A305$^{6.61}$–L555$^{12.64}$–V746$^{16.54}$" (numbers in superscript represent the Ballesteros and Weinstein numbering system) [23], unlike those of other M-PPase subfamilies, such as "L-A-L-L" in *Flavobacterium johnsoniae* H^+-PPase (*Fj*H^+-PPase), "F-A-L-T" in *Carboxydothermus hydrogenoformans* H^+-PPase (*Ch*H^+-PPase) and "M-A-L-M" in *Bacteroides vulgatus* Na^+/H^+-PPase (*Bv*Na^+/H^+-PPase) (Fig. 2c). Residues Ala$^{6.61}$ and Leu$^{12.64}$ are highly conserved in all hydrophobic gates characterized thus far, except for *Tm*Na^+-PPase in which the small hydrophobic residue "Ala$^{6.61}$" is replaced by the small polar residue "Ser$^{6.61}$" as "L-S-L-L." Sequence diversity, differences in ion pore size and other characteristics of the hydrophobic gate might be related to ion selectivity, affecting the ion translocation abilities of M-PPases.

A latch in the exit channel

The salt-bridge interaction of residues E225$^{5.33}$ and R562$^{12.71}$ at the exit channel is highly conserved in plant M-PPases. Previous studies have shown that the E225A and R562A mutations of *Vr*H^+-PPase resulted in decreased enzymatic and proton-pumping activities [35,36], implying that these residues are essential for the PP_i-hydrolytic and proton-pumping activities. The PP_i-hydrolytic and proton-pumping coupling efficiency of the E225A mutant is lower than that of E225H and E225S (Table 2); although the hydrolysis activities of these mutants are similar, the energy requirement for proton release by the E225 mutant may differ from that of the other two mutants [27]. The interaction of E225–R562 has been abolished in the *Vr*H^+-PPase E225A mutant, perhaps affecting proton release. Similar interactions by polar residues have also been found in *Fj*H^+-PPase (residues E175$^{5.33}$ and Y262$^{6.68}$) and *Ch*H^+-PPase (residues H163$^{5.33}$ and T250$^{6.68}$) [23]. We suggest that an essential interaction (which can be a salt-bridge, hydrogen bond, polar interaction, or ion-pair interaction) may be necessary to regulate proton release from the exit channel. Thus, the unique salt-bridge of E225–R562 at the end of the exit channel in *Vr*H^+-PPase may act as a latch to control proton release.

The structural comparison of *Vr*H^+-PPase–2P_i and *Vr*H^+-PPase–P_i complexes and E225 mutants (E225A/E225H) is shown in Fig. 5a. From the differences of side chain orientations of E225 and R562, the dynamic motions of the salt bridge E225–R562 were observed. We suggest a possible sequential movement (steps 1–2–3) of this essential salt bridge at the exit channel, and it might imply the way of proton release (Fig. 6b). Based on the M-PPase catalytic cycle [21] and this *Vr*H^+-PPase study, a mechanism of dynamic molecular motions from 2P_i to P_i state of M-PPase is proposed (Fig. 6b). From 2P_i to P_i state, the latch of E225–R562 will open and close; meanwhile, it will cooperate with the TM12 movement.

In addition, from the observed waters (Fig. 3g, h and i), Wat5, Wat6 and Wat7 were similarly located along the cavity of the exit channel, but the locations of Wat8, Wat9 and Wat10 varied (Fig. S3). Wat8 is located near the corresponding location of the carboxylate group of the glutamic acid (E225) in the P_i leaving state (*Vr*H^+-PPase–P_i complex). Wat9 is close to the carboxylate of the glutamic acid (E225) in

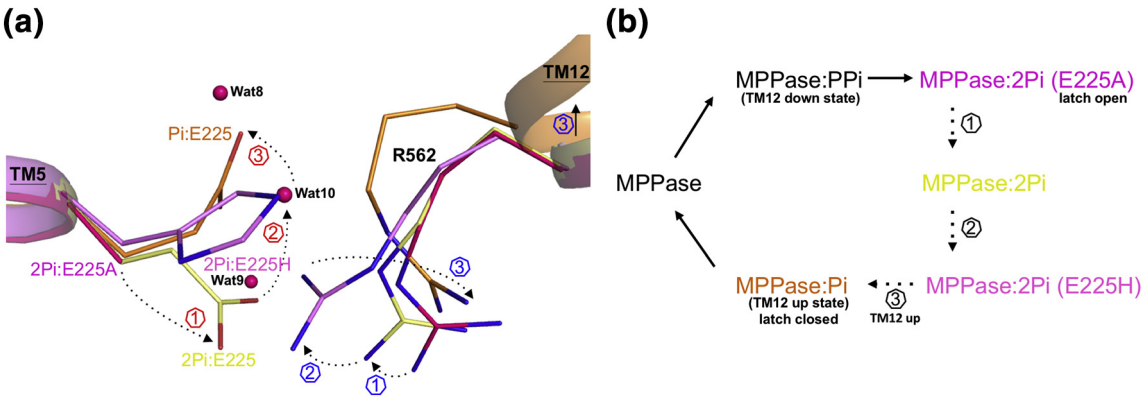

Fig. 5. The latch (E225–R562) at exit channel. (a) Structure superimposition of the *Vr*H^+-PPase–2P_i complex (yellow), *Vr*H^+-PPase–P_i complex (orange), E225A (red) and E225H (purple) mutants. The side-chain movements of E225 and R562 are shown. The sequential molecular movements (arrow 1–2–3) are labeled. (b) The proposed mechanism of the sequential latch open and close from 2P_i to P_i state. Based on the previous studies [21] and this study, the mechanism of M-PPase of the sequential steps (arrow 1–2–3) of latch open and close from 2P_i to P_i state is shown.

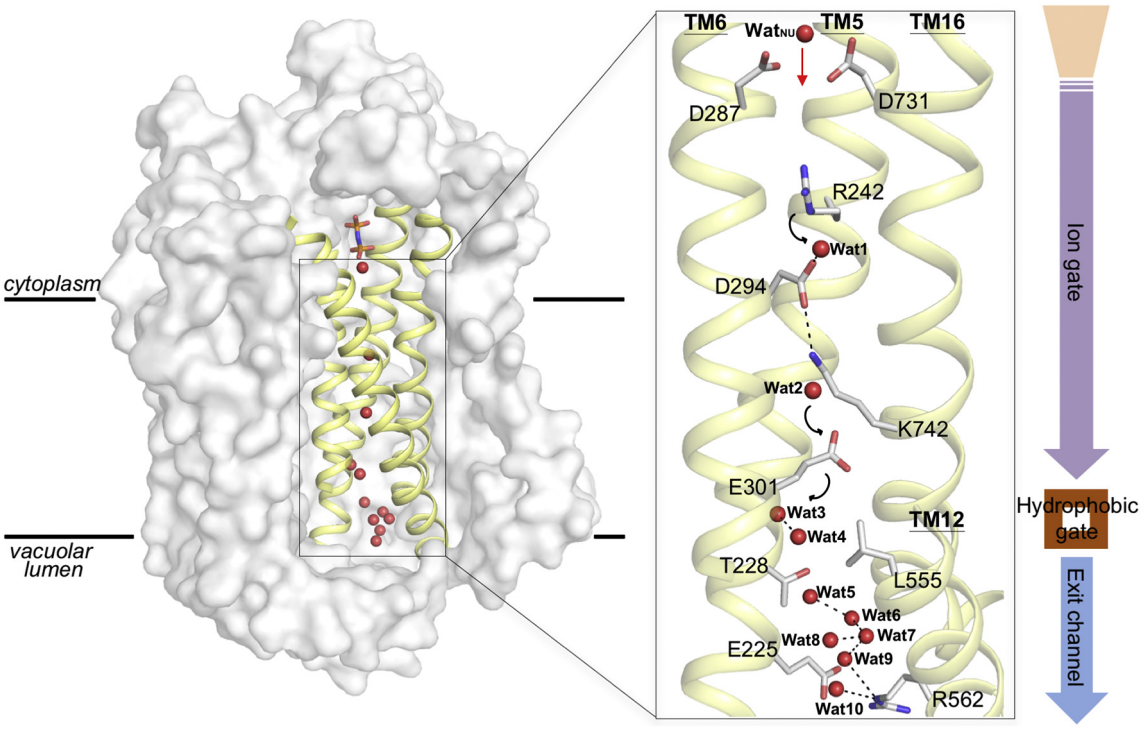

Fig. 6. Water-flow along the ion translocation pathway of *Vr*H$^+$-PPase. Schematic of the water-wire is shown, and it comprised Wat_{nu} and Wat1–Wat10 located inside the four TMs (TMs 5, 6, 12 and 16) from ion gate through hydrophobic gate and to the exit channel. The *Vr*H$^+$-PPase monomer is shown as surface.

the immediate product-bound state (*Vr*H$^+$-PPase–2P_i complex). Wat10 is at the corresponding location of the Nε of the H225 side-chain that might form the hydrogen bond with R562. Thus, Wat8–Wat9–Wat10 (Figs. 3g and 5a) are allocated at the corresponding E225 positions, and it might reflect the possible route of proton release of *Vr*H$^+$-PPase. The opening and closing of the exit channel by the latch and these waters move around the exit channel to mimic the proton release. Moreover, the E225A mutant (Fig. 5) may mimic the exit channel open state of the *Vr*H$^+$-PPase.

Water-flow mimics the proton translocation

For the *Vr*H$^+$-PPase, Wat_{nu}, a nucleophilic water and Wat1/Wat2 were determined in the *Vr*H$^+$-PPase–IDP complex to assist proton transport [20]. These water molecules are located inside the six core TMs (TMs 5–6, 11–12 and 15–16) and buried in the membrane part of the ion translocation pathway. In this study, we have identified this continuous water flow comprising additional Wat3–Wat10 (Fig. 6), which are found at hydrophobic gate and exit channel.

Upon PP_i binding, repositioning of D287 and D731 activates Wat_{nu} to hydrolyze PP_i and initiate proton transfer. The proton is transferred via two acid–base pair residues in the R-D-K-E ion gate by the "Grotthuss-chain" mechanism [37], which is facilitated by two ordered waters (Wat1 and Wat2). Then, Wat3 and Wat4 in the hydrophobic gate imply the possibility of solvation, and the highly conserved L555 forms a hydrophobic barrier that acts as a valve seal. At the exit channel, E225 is located at 12 Å distant from E301, a considerable distance for a proton to cross in the absence of acid–base pair residues. However, we observed a continuous water wire, Wat5–Wat10 along the exit channel. To advance proton transport, these water molecules act like a spout for proton release and are regulated by the essential salt-bridge E225–R562. This continuous water wire from the ion gate through the hydrophobic gate and into the exit channel may reflect the path of proton transfer in *Vr*H$^+$-PPase (Fig. 6).

From M-PPase, the four TMs (TMs 5, 6, 12 and 16) play specific roles in ion translocation. R242 in TM5, representing the first residue of R-D-K-E of the ion gate, may initiate proton transfer. E225 in TM5 is at the way out of the exit channel and cooperated with R562 to regulate the proton release. TM5 might also play a further important role in ion transport through its highly conserved residue R242 and partially conserved residue E225 lying at the start and end points of the ion translocation pathway, respectively.

Materials and Methods

Protein expression of *Vr*H$^+$-PPase

Saccharomyces cerevisiae strain BJ2168 was transformed with the *Vr*H$^+$-PPase gene-carrying plasmid as previously described [38]. The colonies were inoculated into 4 ml of culture medium with 2% (w/v) glucose as a carbon source and incubated at 30 °C and 140 rpm for 1 day. Then, the 4 ml of yeast culture was transferred into 50 ml of culture medium and incubated for 1 day at 30 °C. After 1-day incubation, the 50 ml of yeast culture was transferred into 400 ml of culture medium and incubated for a further 2 days at 30 °C. Cells were collected and transferred to 1 L of culture medium with 2% (w/v) galactose for overexpression for up to 3 days at 30 °C, before harvesting total cells by centrifuging at 2300*g* at 4 °C for 10 min. The harvested cells were washed with wash buffer [100 mM Tris–HCl buffer (pH 9.4), 10 mM 2-mercaptoethanol]. After washing, yeast cell walls were digested with lyticase buffer [100 mM Tris-MES (pH 8.0), 1% (w/v) yeast extract, 2% (w/v) peptone, 1% (w/v) glucose, 13% (w/v) sorbitol, 5 mM 2-mercaptoethanol, and 80,000 units of lyticase] at 37 °C and 140 rpm for 2.5 h and then centrifuged at 2300*g* for 10 min. Finally, the lyticase-treated yeast cells were collected and stored at −80 °C for microsome isolation.

Microsome isolation and protein purification

The lyticase-treated yeast cells were resuspended in lysis buffer [5 mM Tris/EGTA (pH 7.6), 10% (w/v) glycerol, 0.6% (w/v) Tris (base), 0.6% (w/v) ascorbate, 1.5% (w/v) PVP 40,000, 1 mM PMSF and 1 μg/ml pepstatin A] and disrupted by ultrasonication. The homogenate was first centrifuged at 2300*g* for 10 min and then at 126,000*g* for 35 min, both at 4 °C. After ultracentrifugation, the membrane vesicles were resuspended in extraction buffer [25 mM MOPS/KOH (pH 7.0), 400 mM KCl, 4 mM $MgCl_2$, 20% (w/v) glycerol and 1 mM PMSF] and solubilized by using *n*-dodecyl-β-D-maltopyranoside at a protein-to-detergent ratio of 1:2.5. The suspension was gently stirred at 4 °C for 1 h before being centrifuged at 126,000*g* for 35 min. After ultracentrifugation, the supernatant was immediately incubated with Ni^{2+}-NTA beads containing 10 mM imidazole under gentle stirring at 4 °C for 1 h. The supernatant and matrix were injected into the column, washed with wash buffer [25 mM Mops/KOH (pH 7.0), 400 mM KCl, 4 mM $MgCl_2$, 20% (w/v) glycerol, 1 mM PMSF, 0.15% (w/v) *n*-decyl-β-D-maltopyranoside (DM) and 50 mM imidazole], and eluted with elution buffer [25 mM MOPS/KOH (pH 7.0), 400 mM KCl, 4 mM $MgCl_2$, 20% (w/v) glycerol, 1 mM PMSF, 0.15% (w/v) DM and 250 mM imidazole]. The purified *Vr*H$^+$-PPase was transferred to crystallization buffer [25 mM MES (pH 6.5), 400 mM KCl, 4 mM $MgCl_2$, 20% (w/v) glycerol and 0.15% (w/v) DM] and concentrated to 10–20 mg/ml for crystallization.

Site-directed mutagenesis

We used the QuikChange system to design mutagenic primers for generating the single-point-mutated *Vr*H$^+$-PPase cDNA (Table 1). Each 50 μl of reaction sample contained 1× reaction buffer, 50 ng wild-type *Vr*H$^+$-PPase cDNA, 0.2 μM primers, 0.2 mM dNTP mix and 2.5 units of *PfuTurbo* DNA polymerase. The PCR protocol was as follows: (1) an initialization step at 95 °C for 30 s; (2) 16 cycles of a denaturation step at 95 °C for 30 s, an annealing step at 60 °C for 1 min, and an elongation step at 68 °C for 10 min; and (3) a final extension step at 68 °C for 20 min. Each PCR product was treated with 1 μl of the restriction enzyme DpnI (10 U/μl) at 37 °C for 1 h to digest the methylated-parental DNA. After validating cDNAs by DNA sequencing, the successfully mutated *Vr*H$^+$-PPase cDNAs were transformed into *S. cerevisiae* strain BJ2168.

PP_i hydrolytic activity

PP_i hydrolytic activity of *Vr*H$^+$-PPase was measured as the release of P_i from PP_i in a reaction mixture [30 mM Tris/Mes (pH 8.0), 50 mM KCl, 1 mM $MgSO_4$, 250 μM NaF, 1 mM Na_4PP_i, 1.5 μg/ml gramicidin D and 30 μg microsomal protein] incubated at 37 °C for 10 min [39]. After incubation, the reaction was terminated with a coloring solution [125 mM H_2SO_4, 10 mM ascorbic acid, 40 μM potassium antimony (III) oxide tartrate and 500 μM ammonium heptamolybdate]. Released P_i was determined at 850 nm as described previously [40] using a Hitachi U-3900 UV/Vis spectrophotometer.

Proton translocation activity

Proton translocation was measured as the initial rate of fluorescence quenching of acridine orange (excitation wavelength at 490 nm, emission wavelength at 530 nm) as described previously [41]. The reaction mixture for proton translocation measurements contained buffer [5 mM Tris/MES (pH 7.2), 100 mM KCl, 1.5 mM $MgCl_2$, 300 mM sorbitol, 0.2% BSA, 5 μM acridine orange] and 200 μg/ml microsomes. The reaction was initiated by adding 1 mM tetrasodium pyrophosphate (Na_4PP_i). The ionophore, gramicidin D (3 μg/ml), was added at the end of each assay to confirm membrane integrity.

Crystallization and structure determination

Crystallization trials were carried out using the hanging-drop vapor-diffusion method [42]. The *Vr*H$^+$-

PPase–$2P_i$ complex crystals were obtained in 2 days over a reservoir solution at 20 °C containing 100 mM MES (pH 6.5), 250 mM $MgCl_2$, 23% (w/v) PEG2KMME and 10% glycerol, using 0.5 μl of protein drops pre-incubated with 1 mM KH_2PO_4 and 1 mM $SrCl_2$ mixed 1:1 with the reservoir solution. The x-ray diffraction data were collected at the TPS05A and TLS15A beamlines at National Synchrotron Radiation Research Center, Hsinchu, Taiwan. Data were processed by HKL2000 [43]. The *Vr*H^+-PPase–$2P_i$ complex crystals belonged to the monoclinic space group C2, with the cell parameters a = 217.6 Å, b = 88.4 Å, c = 159.1 Å and β = 125.5° (Table 1), and we calculated the Matthew's coefficient to be 3.9 $Å^3$ Da^{-1}, corresponding to a solvent content of 68.4% with two subunits per asymmetric unit [44]. The crystal structure of the *Vr*H^+-PPase–$2P_i$ complex was determined by molecular replacement with MOLREP [45] using the *Vr*H^+-PPase–IDP complex (PDB: 4A01) [20] as a search model. There were two molecules as a dimer per asymmetric unit in the *Vr*H^+-PPase–$2P_i$ complex. The entire crystal structure of the *Vr*H^+-PPase–$2P_i$ complex was completed manually with COOT [46] and refined by PHENIX [47]. The stereochemistry of the protein residues and the secondary structural features were evaluated by PROCHECK [48]. Each monomer of the *Vr*H^+-PPase–$2P_i$ complex contains two P_i, five Mg^{2+} and one K^+ ion. The crystal structure of the *Vr*H^+-PPase–$2P_i$ complex was refined to R/R_{free} 20.7%/24.0% (2.3 Å). Data collection and refinement statistics are listed in Table 1. In addition, crystals of E225A, E225S, E225H, T228D, E301Q, L555M and L555K mutations were all crystallized under conditions similar to that for wild-type *Vr*H^+-PPase–$2P_i$ complex. The crystal structures of all of these mutants are similar to that of wild-type *Vr*H^+-PPase–$2P_i$ complex (Table 1).

Atomic coordinates and structure factors

The atomic coordinates and structure factors of the VrPPase:$2P_i$, and E301Q, L555M, L555K, T228D, E225A, E225S and E225H mutant complexes have been deposited in the Protein Data Bank Japan, http://pdbj.org (PDB IDs 6AFS, 6AFT, 6AFU, 6AFV, 6AFW, 6AFX, 6AFY and 6AFZ).

CRediT authorship contribution statement

Jia-Yin Tsai: Conceptualization, Data curation, Investigation, Writing - original draft, Writing - review & editing. **Kai-Zhi Tang:** Investigation. **Kun-Mou Li:** Investigation. **Bo-Ling Hsu:** Investigation. **Yun-Wei Chiang:** Funding acquisition. **Adrian Goldman:** Writing - review & editing. **Yuh-Ju Sun:** Conceptualization, Data curation, Funding acquisition, Supervision, Writing - original draft, Writing - review & editing.

Acknowledgments

This work was supported by the Ministry of Science and Technology, Taiwan: Grants 105-2627-M-007-005, 106-2627-M-007-008 and 107-2321-B-007-004 (to Y.-J. S.) and 106-2627-M-007-009 (to Y.-W. C.). We thank the National Synchrotron Radiation Research Center for access to beamline TPS05A and TLS15A, and the in-house x-ray facility in the Macromolecular X-ray Crystallographic Center of National Tsing Hua University. We thank the Biophysics core center at the Institute of Biological Chemistry, Academia Sinica.

Author Contributions: Y-J.S. and J-Y.T. designed the research; J-Y.T., K-M.L., B-L.H. and K-Z.T. performed the functional experiments; J-Y.T. and K-M.L. determined the structures; and all authors wrote the paper.

Appendix A. Supplementary data

Supplementary data to this article can be found online at https://doi.org/10.1016/j.jmb.2019.03.009.

Received 16 January 2019;
Received in revised form 26 February 2019;
Accepted 3 March 2019
Available online 13 March 2019

Keywords:
membrane protein;
primary ion pump;
pyrophosphate hydrolysis;
proton translocation;
x-ray crystallography

Abbreviations used:
M-PPases, membrane-embedded pyrophosphatases; TMs, transmembrane helices; R-D-K-E, R242–D294–K742–E301; DM, *n*-decyl-β-D-maltopyranoside.

References

[1] A.A. Baykov, A.M. Malinen, H.H. Luoto, R. Lahti, Pyrophosphate-fueled Na^+ and H^+ transport in prokaryotes, Microbiol. Mol. Biol. Rev. 77 (2013) 267–276.
[2] S. Segami, M. Asaoka, S. Kinoshita, M. Fukuda, Y. Nakanishi, M. Maeshima, Biochemical, structural and physiological characteristics of vacuolar H^+-pyrophosphatase, Plant Cell Physiol. 59 (2018) 1300–1308.
[3] M. Maeshima, Vacuolar H^+-pyrophosphatase, Biochim. Biophys. Acta 1465 (2000) 37–51.
[4] G.A. Belogurov, M.V. Turkina, A. Penttinen, S. Huopalahti, A. A. Baykov, R. Lahti, H^+-pyrophosphatase of *Rhodospirillum rubrum*. High yield expression in *Escherichia coli* and

identification of the Cys residues responsible for inactivation my mersalyl, J. Biol. Chem. 277 (2002) 22209–22214.
[5] M. Maeshima, H(+)-translocating inorganic pyrophosphatase of plant vacuoles. Inhibition by Ca^{2+}, stabilization by Mg^{2+} and immunological comparison with other inorganic pyrophosphatases, Eur. J. Biochem. 196 (1991) 11–17.
[6] A. Fraichard, C. Trossat, E. Perotti, A. Pugin, Allosteric regulation by Mg^{2+} of the vacuolar H(+)-PPase from Acer pseudoplatanus cells. Ca^{2+}/Mg^{2+} interactions, Biochimie 78 (1996) 259–266.
[7] A. Sosa, H. Ordaz, I. Romero, H. Celis, Mg^{2+} is an essential activator of hydrolytic activity of membrane-bound pyrophosphatase of *Rhodospirillum rubrum*, Biochem. J. 283 (Pt 2) (1992) 561–566.
[8] M. Baltscheffsky, A. Schultz, H. Baltscheffsky, H^+-proton-pumping inorganic pyrophosphatase: a tightly membrane-bound family, FEBS Lett. 452 (1999) 121–127.
[9] M.T. McIntosh, A.B. Vaidya, Vacuolar type H^+ pumping pyrophosphatases of parasitic protozoa, Int. J. Parasitol. 32 (2002) 1–14.
[10] A. Serrano, J.R. Perez-Castineira, H. Baltscheffsky, M. Baltscheffsky, Proton-pumping inorganic pyrophosphatases in some archaea and other extremophilic prokaryotes, J. Bioenerg. Biomembr. 36 (2004) 127–133.
[11] A. Serrano, J.R. Perez-Castineira, M. Baltscheffsky, H. Baltscheffsky, H^+-PPases: yesterday, today and tomorrow, IUBMB Life 59 (2007) 76–83.
[12] Y. Nakanishi, T. Saijo, Y. Wada, M. Maeshima, Mutagenic analysis of functional residues in putative substrate-binding site and acidic domains of vacuolar H^+-pyrophosphatase, J. Biol. Chem. 276 (2001) 7654–7660.
[13] G.A. Belogurov, R. Lahti, A lysine substitute for K^+. A460K mutation eliminates K^+ dependence in H^+-pyrophosphatase of *Carboxydothermus hydrogenoformans*, J. Biol. Chem. 277 (2002) 49651–49654.
[14] E. Artukka, H.H. Luoto, A.A. Baykov, R. Lahti, A.M. Malinen, Role of the potassium/lysine cationic center in catalysis and functional asymmetry in membrane-bound pyrophosphatases, Biochem. J. 475 (2018) 1141–1158.
[15] H.H. Luoto, E. Nordbo, A.M. Malinen, A.A. Baykov, R. Lahti, Evolutionarily divergent, Na^+-regulated H^+-transporting membrane-bound pyrophosphatases, Biochem. J. 467 (2015) 281–291.
[16] R.K. Schilling, M. Tester, P. Marschner, D.C. Plett, S.J. Roy, AVP1: one protein, many roles, Trends Plant Sci. 22 (2017) 154–162.
[17] G.A. Pizzio, J. Paez-Valencia, A.S. Khadilkar, K. Regmi, A. Patron-Soberano, S. Zhang, et al., Arabidopsis type I proton-pumping pyrophosphatase expresses strongly in phloem, where it is required for pyrophosphate metabolism and photosynthate partitioning, Plant Physiol. 167 (2015) 1541–1553.
[18] R.A. Gaxiola, K. Regmi, J. Paez-Valencia, G. Pizzio, S. Zhang, Plant H(+)-PPases: reversible enzymes with contrasting functions dependent on membrane environment, Mol. Plant 9 (2016) 317–319.
[19] Y.D. Hsu, Y.F. Huang, Y.J. Pan, L.K. Huang, Y.Y. Liao, W.H. Lin, et al., Regulation of H(+)-pyrophosphatase by 14-3-3 proteins from *Arabidopsis thaliana*, J. Membr. Biol. 251 (2018) 263–276.
[20] S.M. Lin, J.Y. Tsai, C.D. Hsiao, Y.T. Huang, C.L. Chiu, M.H. Liu, et al., Crystal structure of a membrane-embedded H^+-translocating pyrophosphatase, Nature 484 (2012) 399–403.
[21] K.M. Li, C. Wilkinson, J. Kellosalo, J.Y. Tsai, T. Kajander, L.J. Jeuken, et al., Membrane pyrophosphatases from *Thermotoga maritima* and *Vigna radiata* suggest a conserved coupling mechanism, Nat. Commun. 7 (2016), 13596.
[22] J. Kellosalo, T. Kajander, K. Kogan, K. Pokharel, A. Goldman, The structure and catalytic cycle of a sodium-pumping pyrophosphatase, Science 337 (2012) 473–476.
[23] J.Y. Tsai, J. Kellosalo, Y.J. Sun, A. Goldman, Proton/sodium pumping pyrophosphatases: the last of the primary ion pumps, Curr. Opin. Struct. Biol. 27C (2014) 38–47.
[24] P. Heikinheimo, V. Tuominen, A.K. Ahonen, A. Teplyakov, B. S. Cooperman, A.A. Baykov, et al., Toward a quantum-mechanical description of metal-assisted phosphoryl transfer in pyrophosphatase, Proc. Natl. Acad. Sci. U. S. A. 98 (2001) 3121–3126.
[25] A.A. Baykov, N.P. Bakuleva, P.A. Rea, Steady-state kinetics of substrate hydrolysis by vacuolar H(+)-pyrophosphatase. A simple three-state model, Eur. J. Biochem. 217 (1993) 755–762.
[26] Y.J. Pan, C.H. Lee, S.H. Hsu, Y.T. Huang, C.H. Lee, T.H. Liu, et al., The transmembrane domain 6 of vacuolar H^+-pyrophosphatase mediates protein targeting and proton transport, Biochim. Biophys. Acta 1807 (2011) 59–67.
[27] M. Asaoka, S. Segami, M. Maeshima, Identification of the critical residues for the function of vacuolar H^+-pyrophosphatase by mutational analysis based on the 3D structure, J. Biochem. 156 (2014) 333–344.
[28] H. Luecke, H.T. Richter, J.K. Lanyi, Proton transfer pathways in bacteriorhodopsin at 2.3 angstrom resolution, Science 280 (1998) 1934–1937.
[29] V. Sharma, M. Wikstrom, V.R. Kaila, Dynamic water networks in cytochrome cbb3 oxidase, Biochim. Biophys. Acta 1817 (2012) 726–734.
[30] M. Pellegrini-Calace, T. Maiwald, J.M. Thornton, PoreWalker: a novel tool for the identification and characterization of channels in transmembrane proteins from their three-dimensional structure, PLoS Comput. Biol. 5 (2009), e1000440.
[31] M. Hirono, Y. Nakanishi, M. Maeshima, Essential amino acid residues in the central transmembrane domains and loops for energy coupling of *Streptomyces coelicolor* A3(2) H^+-pyrophosphatase, Biochim. Biophys. Acta 1767 (2007) 930–939.
[32] J.D. Ho, R. Yeh, A. Sandstrom, I. Chorny, W.E. Harries, R.A. Robbins, et al., Crystal structure of human aquaporin 4 at 1.8 A and its mechanism of conductance, Proc. Natl. Acad. Sci. U. S. A. 106 (2009) 7437–7442.
[33] A. Kirscht, S.S. Kaptan, G.P. Bienert, F. Chaumont, P. Nissen, B.L. de Groot, et al., Crystal structure of an ammonia-permeable aquaporin, PLoS Biol. 14 (2016), e1002411.
[34] C.M. Suomivuori, A.P. Gamiz-Hernandez, D. Sundholm, V.R. I. Kaila, Energetics and dynamics of a light-driven sodium-pumping rhodopsin, Proc. Natl. Acad. Sci. U. S. A. 114 (2017) 7043–7048.
[35] Y.Y. Hsiao, Y.J. Pan, S.H. Hsu, Y.T. Huang, T.H. Liu, C.H. Lee, et al., Functional roles of arginine residues in mung bean vacuolar H^+-pyrophosphatase, Biochim. Biophys. Acta 1767 (2007) 965–973.
[36] R.C. Van, Y.J. Pan, S.H. Hsu, Y.T. Huang, Y.Y. Hsiao, R.L. Pan, Role of transmembrane segment 5 of the plant vacuolar H^+-pyrophosphatase, Biochim. Biophys. Acta 1709 (2005) 84–94.
[37] N. Agmon, The Grotthuss mechanism, Chem. Phys. Lett. 244 (1995) 456–462.
[38] Y.Y. Hsu, P.F. Hsiao, S.M. Liu, Y.Y. Lin, R.L. Pan Luo, Purification, characterization, and spectral analyses of

histidine-tagged vacuolar H^+-pyrophosphatase expressed in yeast, Bot. Stud. 50 (2009) 291–301.
[39] C.H. Lee, Y.W. Chen, Y.T. Huang, Y.J. Pan, S.M. Lin, L.K. Huang, et al., Functional investigation of transmembrane helix 3 in H(+)-translocating pyrophosphatase, J. Membr. Biol. 246 (2013) 959–966.
[40] G. Bartolommei, M.R. Moncelli, F. Tadini-Buoninsegni, A method to measure hydrolytic activity of adenosinetriphosphatases (ATPases), PLoS One 8 (2013), e58615.
[41] R.G. Zhen, E.J. Kim, P.A. Rea, Acidic residues necessary for pyrophosphate-energized pumping and inhibition of the vacuolar H^+-pyrophosphatase by *N,N*-dicyclohexylcarbodiimide, J. Biol. Chem. 272 (1997) 22340–22348.
[42] A. McPherson, Current approaches to macromolecular crystallization, Eur. J. Biochem. 189 (1990) 1–23.
[43] Z. Otwinowski, W. Minor, Processing of x-ray diffraction data collected in oscillation mode, Methods Enzymol. 276 (1997) 307–326.
[44] B.W. Matthews, Solvent content of protein crystals, J. Mol. Biol. 33 (1968) 491–497.
[45] A. Vagin, A. Teplyakov, MOLREP: an automated program for molecular replacement, J. Appl. Crystallogr. 50 (1997) 1022–1025.
[46] P. Emsley, B. Lohkamp, W.G. Scott, K. Cowtan, Features and development of Coot, Acta Crystallogr. D Biol. Crystallogr. 66 (2010) 486–501.
[47] P.D. Adams, P.V. Afonine, G. Bunkoczi, V.B. Chen, I.W. Davis, N. Echols, et al., PHENIX: a comprehensive Python-based system for macromolecular structure solution, Acta Crystallogr. D Biol. Crystallogr. 66 (2010) 213–221.
[48] R.A. Laskowski, J.A. Rullmannn, M.W. MacArthur, R. Kaptein, J.M. Thornton, AQUA and PROCHECK-NMR: programs for checking the quality of protein structures solved by NMR, J. Biomol. NMR 8 (1996) 477–486.